

Supplementary Information

Dynamics and hydration explain failed functional transformation in dehalogenase design

Jan Sykora^{1†}, Jan Brezovsky^{2†}, Tana Koudelakova^{2†}, Maryna Lahoda³, Andrea Fortova², Tatsiana Chernovets¹, Radka Chaloupkova², Veronika Stepankova², Zbynek Prokop^{2,4}, Ivana Kuta Smatanova³, Martin Hof^{1*}, Jiri Damborsky^{2,4*}

¹ J. Heyrovský Institute of Physical Chemistry ASCR, v. v. i., Dolejškova 3, 182 23 Prague 8, Czech Republic

² Loschmidt Laboratories, Department of Experimental Biology and Research Centre for Toxic Compounds in the Environment RECETOX, Faculty of Science, Masaryk University, Kamenice 5/A13, 625 00 Brno, Czech Republic

³ Faculty of Science, University of South Bohemia in Ceske Budejovice, Branisovska 31, 37005 Ceske Budejovice and Institute of Nanobiology and Structural Biology ASCR, Zamek 136, 37333 Nove Hradky, Czech Republic

⁴ International Clinical Research Center, St. Anne's University Hospital Brno, Pekarska 53, 656 91 Brno, Czech Republic

†These authors contributed equally to this work

*To whom correspondence should be addressed. E-mail: martin.hof@jh-inst.cas.cz, jiri@chemi.muni.cz

Table of contents

Supplementary note.....	3
Molecular modeling.....	3
Supplementary results.....	6
Supplementary Figure 1. Circular dichroism spectra of studied enzymes.....	6
Supplementary Figure 2. Comparison of the residues involved in the transplanted.	7
Supplementary Figure 3. Superposition of the catalytic pentads.....	8
Supplementary Figure 4. MALDI-TOF MS spectra of DhaA12 and DhaA12-coumarin complex.....	9
Supplementary Figure 5. Acrylamide quenching of coumarin fluorescence for the haloalkane dehalogenase variants.	10
Supplementary Figure 6. Structural formula of the fluorescent coumarin probe.	11
Supplementary Figure 7. Two lowest-energy conformations of the coumarin probe.	12
Supplementary Figure 8. Three lowest-energy conformations of the covalent linker.....	13
Supplementary Figure 9. Five reactive binding modes of the probe bound in DbjA.	14
Supplementary Figure 10. Three reactive binding modes of the probe bound in DhaA.	15
Supplementary Figure 11. Five reactive binding modes of the probe bound in DhaA12.	16
Supplementary Table 1. Characteristics of enzymes used in this study.	17
Supplementary Table 2. Enantioselectivity of wild type and variants with β -bromoalkanes and α -bromoester.	18
Supplementary Table 3. Data collection and refinement.....	19
statistics for the crystal structure of DhaA12.....	19
Supplementary Table 4. Parameters characterizing the overall time-dependent fluorescence shift.	20
Supplementary Table 5. Parameters describing the dynamics and hydration of wild types and DhaA12 mutant.....	21
Supplementary Table 6. Variable residues in the second and the third shell of the active sites of DbjA and DhaA12.....	22
Supplementary Table 7. Atom types and charges for the fluorescent probe used in the simulations.....	23
Supplementary Table 8. Atom types and charges for the covalent linker bound to the aspartic acid residue used in the simulations.	24
Supplementary Table 9. Binding energies of individual binding modes of the fluorescent probe.	25
Supplementary references	26

Supplementary note

Molecular modeling

Preparation of structures for molecular modeling. Crystal structures of the haloalkane dehalogenases were obtained from RSCB PDB database using following accession codes: 1CQW (DhaA), 3SK0 (DhaA12) and 3A2M (DbaA). The catalytic histidine was substituted by phenylalanine in all protein structures and the mutations Val172Ala, Ile209Leu and Gly292Ala were modeled to the crystal structure of DhaA to achieve correspondence with the experimentally used haloalkane dehalogenase DhaA from the strain NCIMB13064 (DDBJ/GenBank/EMBL accession no. AF060871). All mutations were designed in PyMOL 1.4.1 (Schrödinger). Hydrogen atoms were added to the protein structures using H++ server at pH 7.5¹.

Molecular docking. The fluorescent probe consisting of coumarin 120 dye carrying covalent alkyl-halogen linker (Supplementary Fig. 6a) was built in PyMOL 1.4.1. The geometry of probe molecule was optimized using AM1 semi-empirical quantum chemical method² implemented in the program MOPAC2009 (Stewart Computational Chemistry). The structures of the enzymes and the fluorescent probe were prepared for docking calculation by MGLTools 1.5.0³. The fluorescent probe was docked into the active sites of all three studied enzymes using the program AUTODOCK 3.05⁴. The atomic and electrostatic maps were calculated using AUTOGRID 3.06⁴. Range of grid maps was set to 95 × 95 × 95 grid points with spacing 0.25 Å centered on CG atom of substituted phenylalanine to cover the whole active site and the main tunnel of both enzymes. In total, 250 docking calculations were performed employing the Lamarckian Genetic Algorithm with the following parameters: initial population size 150, maximum of 1.5 × 10⁶ energy evaluations and 27,000 generations, elitism value 1, mutation rate 0.02 and cross-over rate 0.8. The local search was based on the pseudo Solis and Wets algorithm with a maximum of 300 iterations per local search⁵. The final orientations from each docking were clustered with a clustering tolerance for the root-mean-square positional deviation of 2 Å.

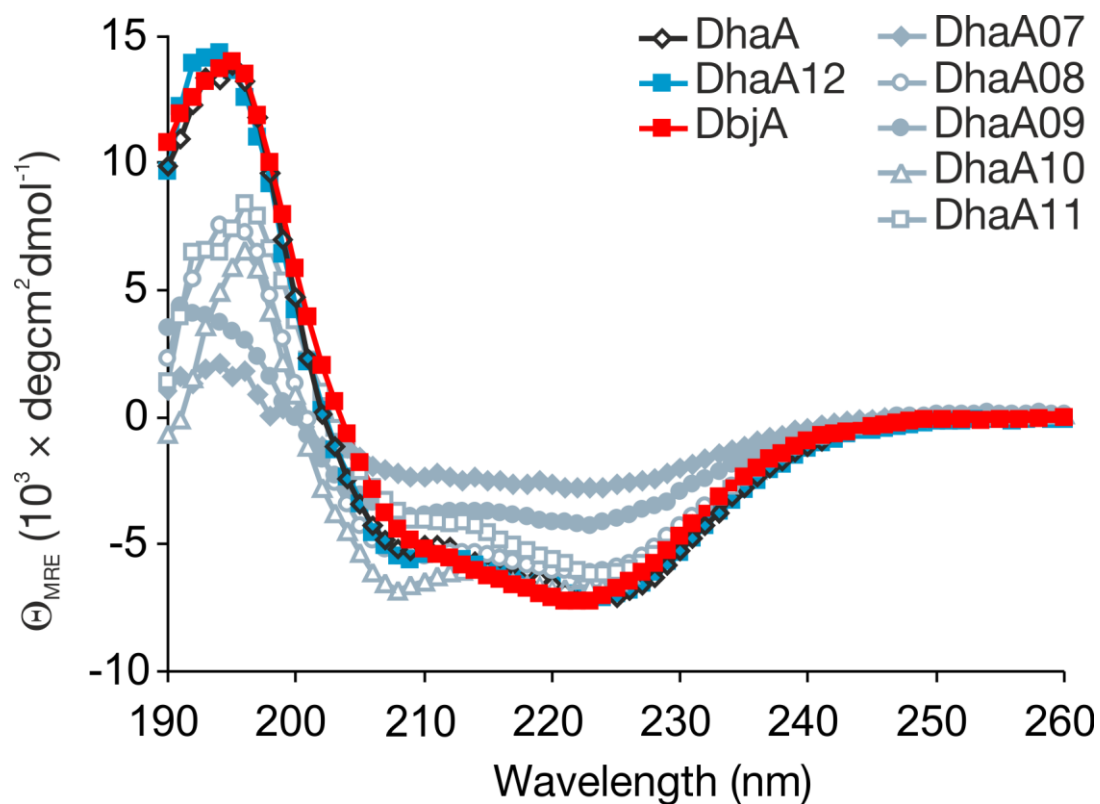
Parameterization of modified amino acid residue for molecular dynamics simulation. The novel residue representing the fluorescent probe covalently bound to the nucleophile of an aspartic acid (Supplementary Fig. 6b) was parameterized by analogy with the Cornell et al. force field⁶. The only exception was the aromatic oxygen that was present in the moiety of fluorescent probe. The required parameters were obtained from the VanBeek et al⁷. The novel residue was constructed from two fragments (i) the coumarin probe capped with N-methylamide (NME) residue (Supplementary Fig. 7), and (ii) the covalent linker capped with acetyl (ACE) residue covalently bound to the aspartic acid residue capped with NME and ACE

residues (Supplementary Fig. 8). The coumarin fragment was modeled in two lowest-energy conformations (Supplementary Fig. 7), while the second fragment was modeled in three lowest-energy conformations keeping the helical conformation of the aspartic acid residue (Supplementary Fig. 8). The geometry of all lowest-energy conformations were energy minimized with MP2/6-31G* wave function using Gaussian09 program revision C.01 (Gaussian, 2009). The partial atomic charges of the novel residue were obtained using RESP ESP charge Derive 2.0 server^{8,9}, with HF/6-31G* level of theory. The charges on the fragments were developed employing RESP-A1A charge model, using multi-conformation multi-orientation RESP fits. During the fitting procedure, the charges on the capping NME and ACE residues were constrained to zero. The charges on the four peptide bond atoms (N43, H44, C45 and O46) of the second fragment were constrained to the values corresponding to the charges on respective atoms of the electro-neutral residues from the Cornell et al. force field⁶. The charges and atom types for both fragments are provided in the Supplementary Table 7 and Supplementary Table 8.

Molecular dynamics simulation. The covalently bound alkyl-enzyme intermediates were manually modeled from the enzyme-substrate complexes obtained from the docking calculations. All enzyme-substrate complexes complying with the basic geometrical prerequisites of S_N2 reaction in the haloalkane dehalogenases¹⁰ were selected (Supplementary Fig. 9-11), and the alkyl-enzyme intermediates were prepared by deleting the chloride atom and placing the carbon atom 1 Å closer to the nucleophile oxygen atom of the aspartic acid residue 106 (DhaA and DhaA12) and 103 (DbjA). Water molecules from the crystal structure were added to the systems to their original positions with the exception of water molecules overlapping with the docked probes. The systems were neutralized by adding 16, 21 and 7 Na⁺ ions to DhaA, DhaA12 and DbjA complexes, respectively, using Tleap module of AmberTools11 (University of California, 2010). Using the same module, an octahedron of TIP3P water molecules¹¹ was added to the distance of 10 Å from any solute atom in the systems. Energy minimization and MD simulations were carried out in PMEMD module of AMBER11 (University of California, 2010) using ff99SB force field¹². The investigated systems were minimized by 500 steps of steepest descent followed by 500 steps of conjugate gradient in five rounds of decreasing harmonic restraints. The restraints were applied as follows: 500 kcal.mol⁻¹.Å⁻² on all heavy atoms of protein, and then 500, 125, 25 and 0 kcal.mol⁻¹.Å⁻² on backbone atoms only. The consequent MD simulations employed periodic boundary conditions, the particle mesh Ewald method for treatment of the electrostatic interactions^{13,14}, 10 Å cutoff for nonbonded interactions, and 2 fs time step with the SHAKE algorithm to fix all bonds containing hydrogens¹⁵. Equilibration simulations consisted of two steps: (i) 20 ps of gradual heating from 0 to 300 K under constant volume, using a Langevin

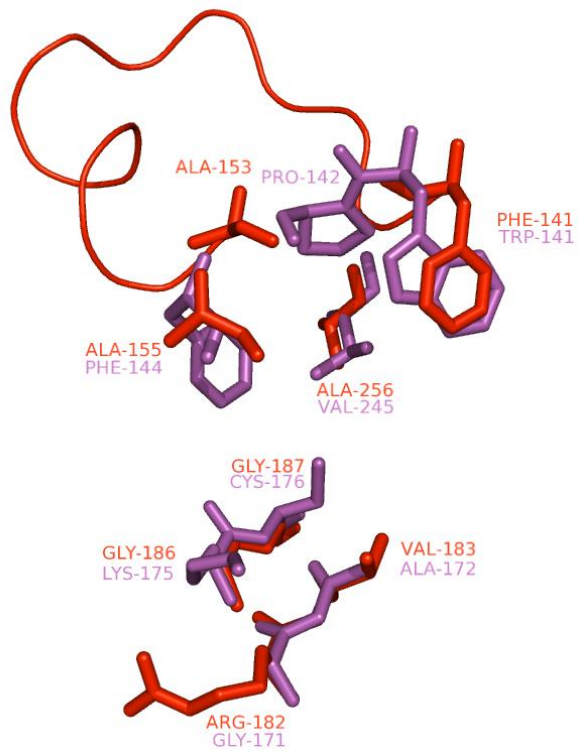
thermostat with collision frequency of 1.0 ps^{-1} , and with harmonic restraints of $5.0 \text{ kcal.mol}^{-1}.\text{\AA}^{-2}$ on the position of all protein atoms, and (ii) 2000 ps of unrestrained MD at 300 K using the Langevin thermostat, and constant pressure of 1.0 bar using pressure coupling constant of 1.0 ps. Finally, production MD simulations were run for 50 ns with the same settings as the second step of equilibration MD. Coordinates were saved in 5 ps interval, and the trajectories were analyzed using Ptraj and Cpptraj modules of AmberTools11, and visualized in Pymol 1.4.1 and VMD 1.8.9¹⁶. The average binding energies of each binding mode were evaluated using Molecular-Mechanics/Generalized-Born Surface Area^{17,18}. Every second frame from the equilibrated part of the molecular dynamics trajectories was selected for the analysis. The following settings were used for the calculation: PBradii were set to mbondi2 and Generalized-Born model to 5¹⁸. The analysis was performed with MMPBSA.py python script of AmberTools11. The binding modes with the lowest energies were then selected for the detailed analysis of each system (Supplementary Table 9).

Supplementary results

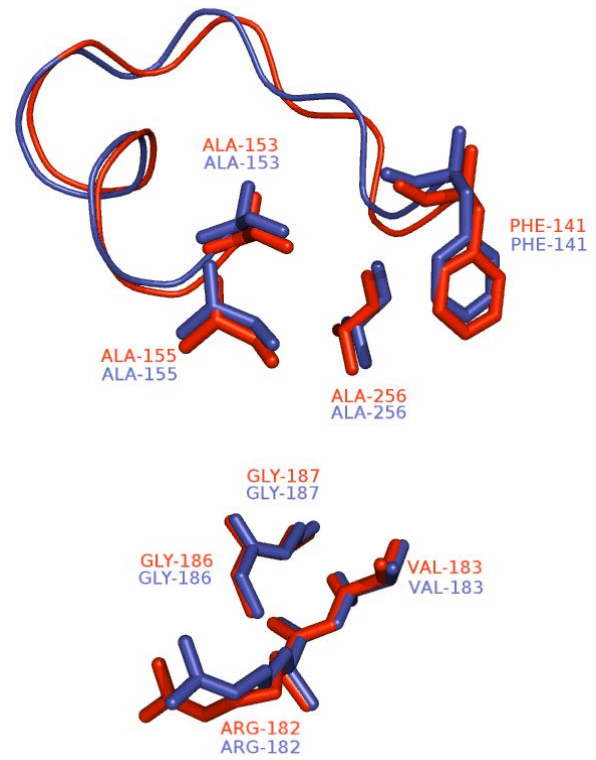


Supplementary Figure 1. Circular dichroism spectra of studied enzymes. All enzymes except DhaA07 and DhaA09 exhibited circular dichroism spectra typical of folded α/β -proteins with a predominately α -helical content. Collected circular dichroism data are expressed in terms of the mean residue ellipticity (Θ_{MRE}).

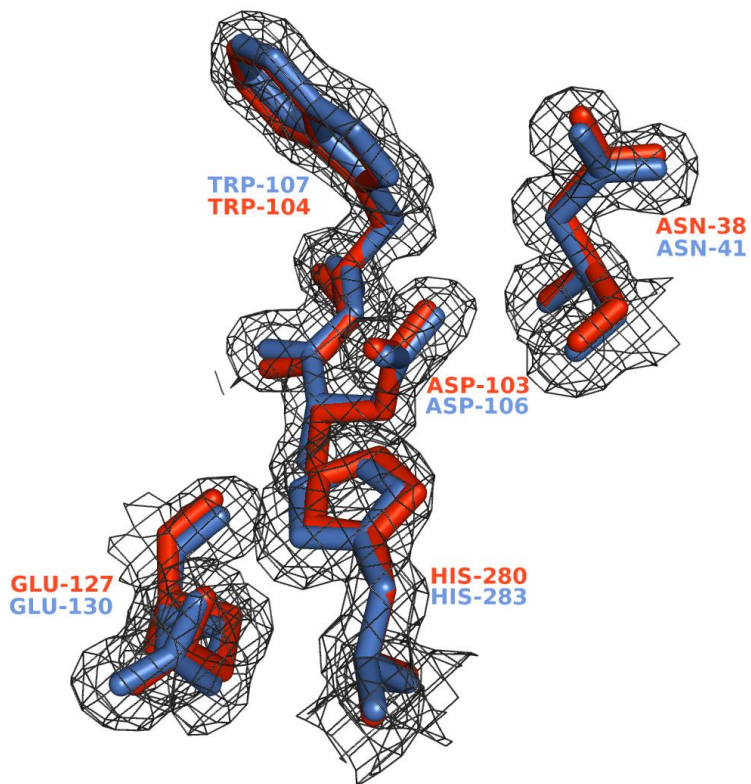
a



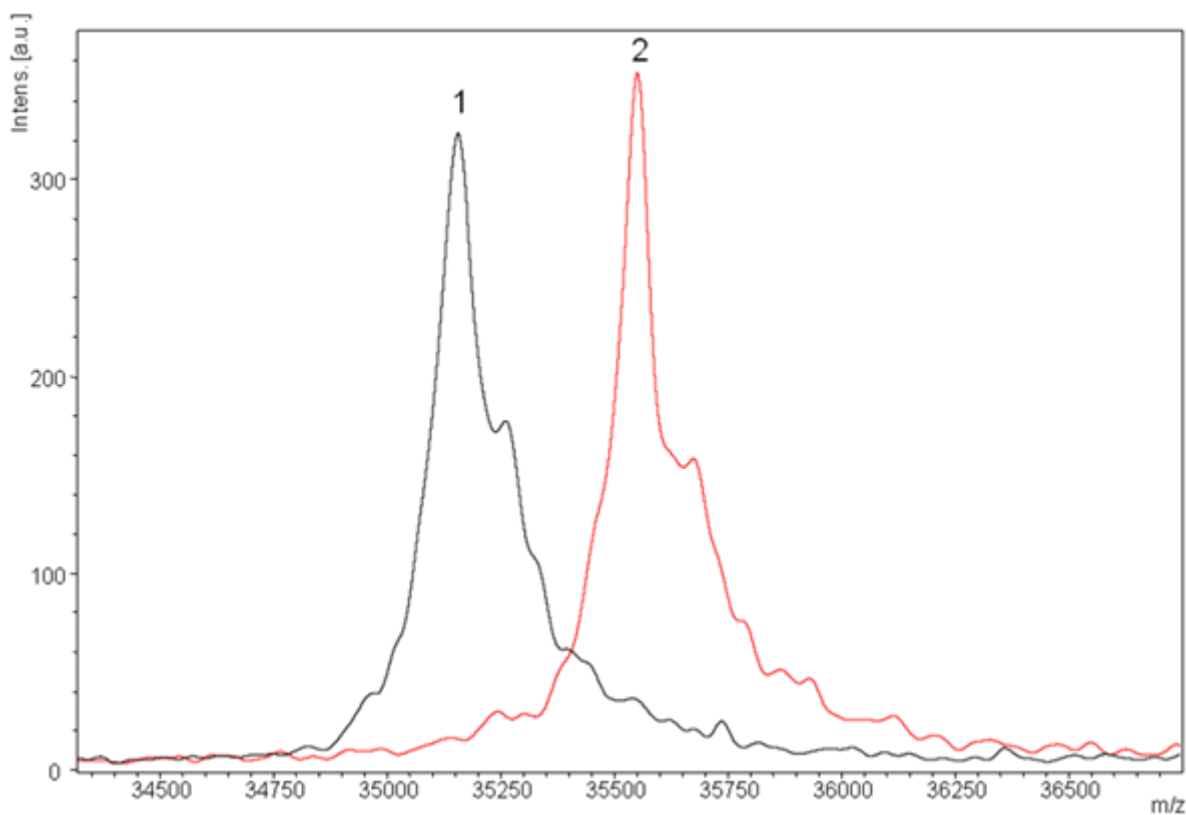
b



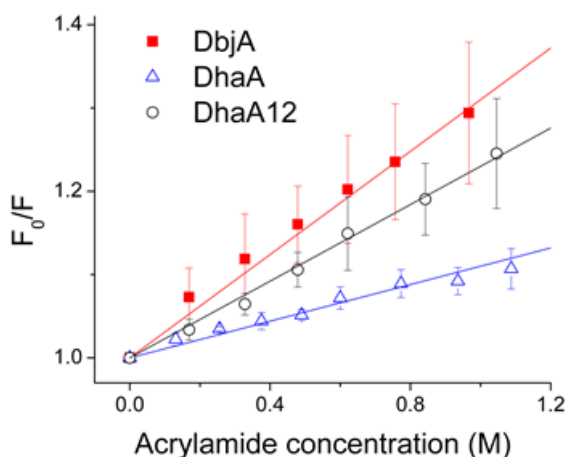
Supplementary Figure 2. Comparison of the residues involved in the transplantation. (a) Active site and tunnel lining residues variable between DbjA (red) and DhaA (magenta). (b) Residues transplanted from DbjA (red) to DhaA12 (blue). EBR fragment is show as ribbon.



Supplementary Figure 3. Superposition of the catalytic pentads. Pentads of DhaA12 (in blue) and DbjA (in red) are represented by sticks. The 2Fo-Fc electron density map of the DhaA12 pentad contoured at 1σ represented by mesh.

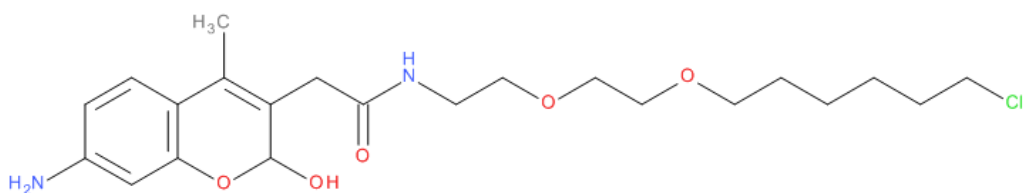


Supplementary Figure 4. MALDI-TOF MS spectra of DhaA12 and DhaA12-coumarin complex. Black spectrum of the free enzyme (peak 1) is compared with red spectrum of the enzyme-probe complex (peak 2). Seven consecutive mass spectra were recorded for each sample and average mass values were calculated ($RSD \leq 0.1\%$). Difference of average masses of enzymes and enzyme-probe complex corresponds to the mass of the coumarin probe. The proteins contain the point mutation in the catalytic histidine His283Phe.

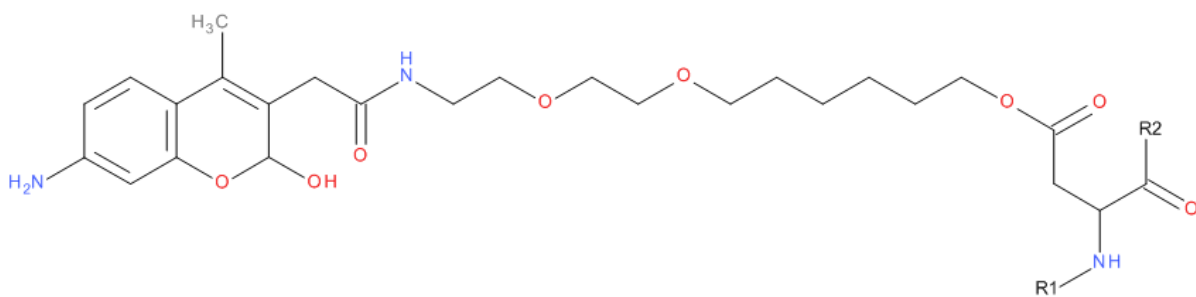


Supplementary Figure 5. Acrylamide quenching of coumarin fluorescence for the haloalkane dehalogenase variants. Stern-Volmer plots for DbjA (■), DhaA (△) and DhaA12 (○) provided Stern-Volmer constants of $0.29 \pm 0.04 \text{ M}^{-1}$, $0.11 \pm 0.02 \text{ M}^{-1}$ and $0.23 \pm 0.06 \text{ M}^{-1}$ respectively. The linearity of those graphs indicates that those enzymes are specifically labeled. The accessibility of the coumarin dye to the acrylamide molecules is substantially higher in the case of the mutants DbjA and DhaA12 than in the case of DhaA. Stern-Volmer constant for DbjA and DhaA12 are comparable, confirming the fact that the tunnel architecture of these enzymes is similar. The emission spectra recorded before and after the quenching procedure did not show any differences for all herein investigated mutants further indicating that the coumarin dye possesses single location within the protein scaffold. Three experiments were performed for DhaA and DbjA, and duplicate measurements were carried out in the case of DhaA12. Data represent mean values \pm s.d.

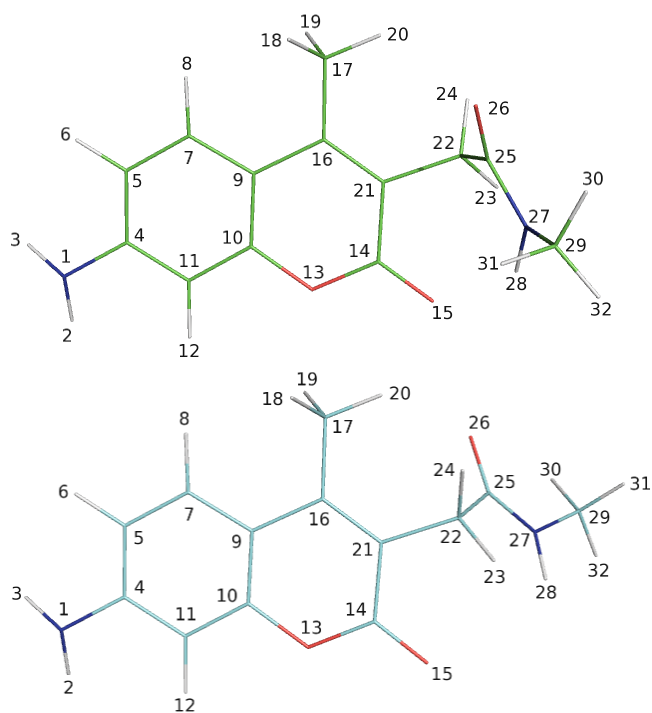
a



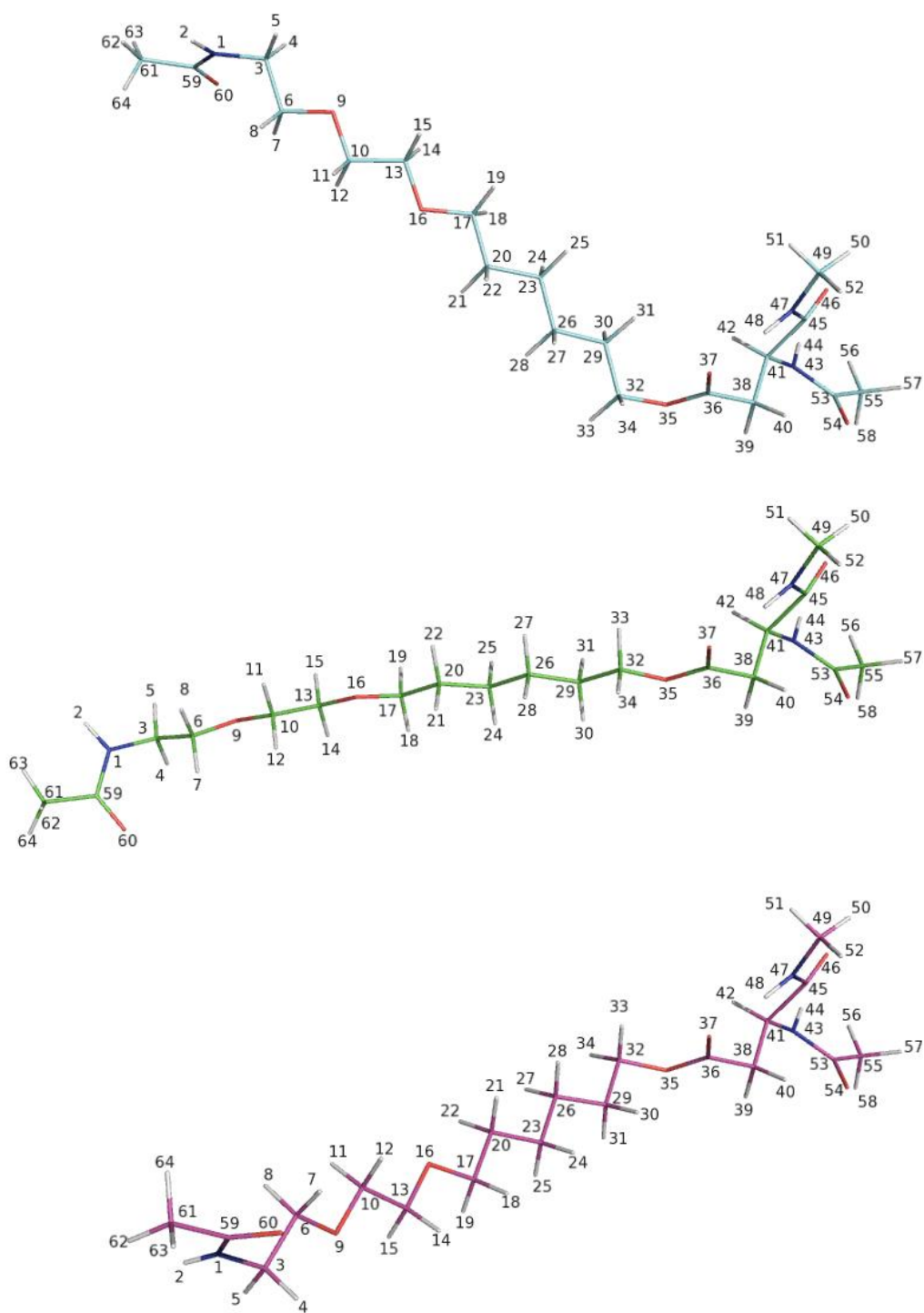
b



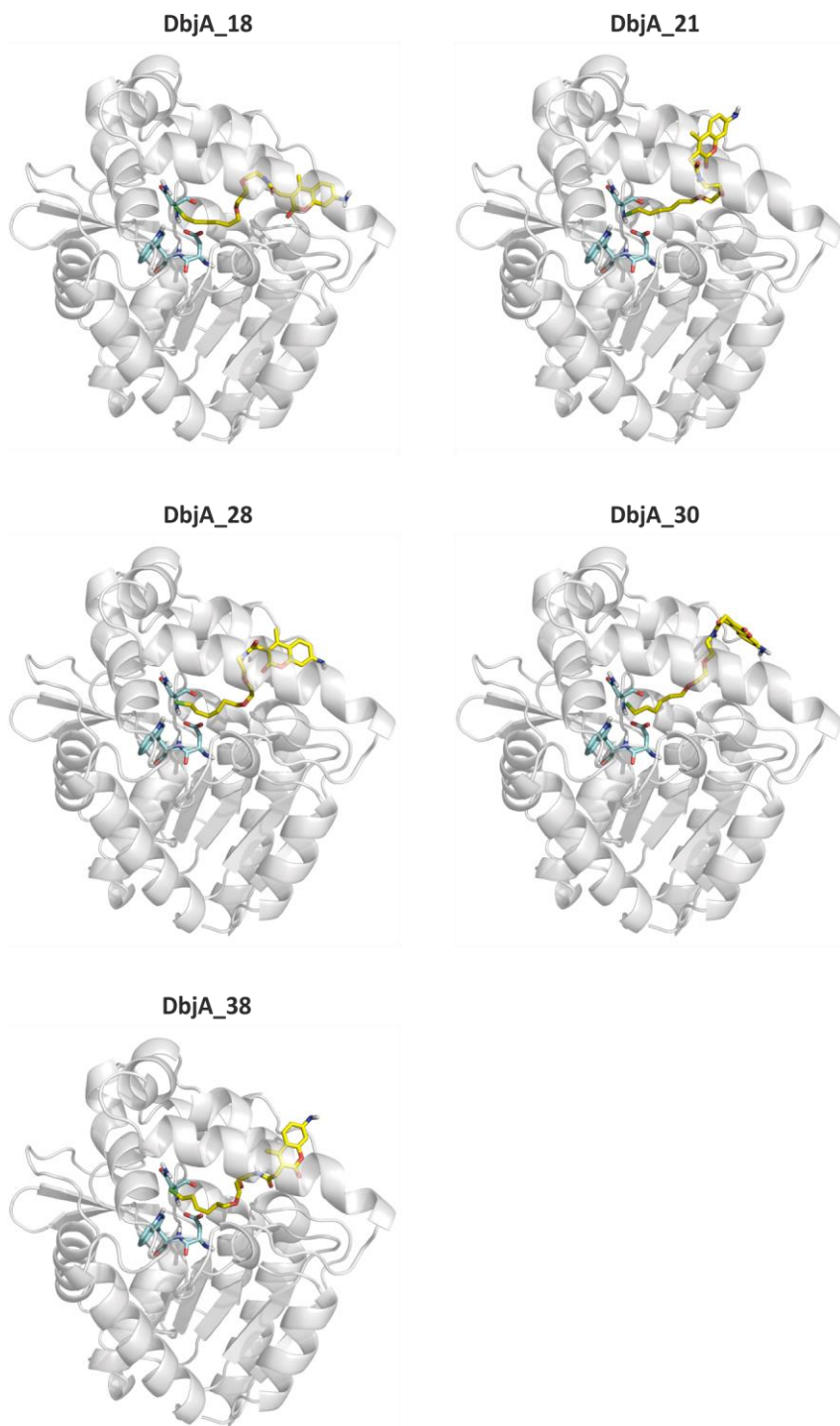
Supplementary Figure 6. Structural formula of the fluorescent coumarin probe. Unbound form (a) and its alkyl-intermediate complex with aspartic acid (b).



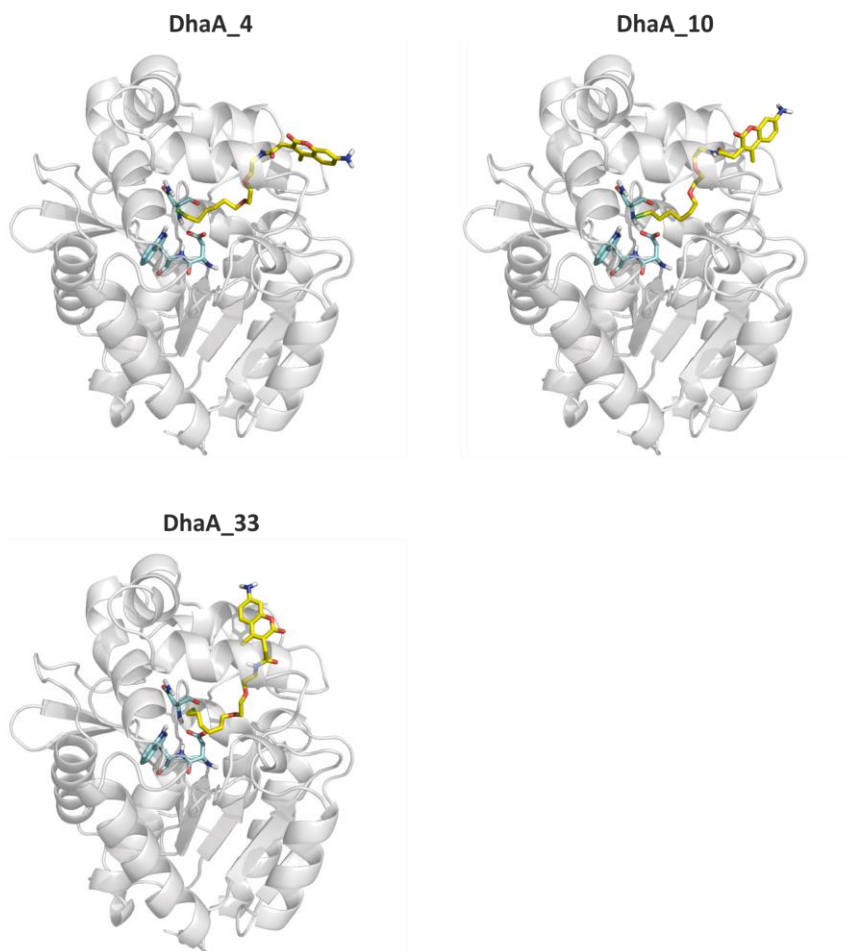
Supplementary Figure 7. Two lowest-energy conformations of the coumarin probe. Probe is capped with NME residue (atoms 27-32) employed for the fragment parameterization. The atoms are numbered in concert with Supplementary Table 7.



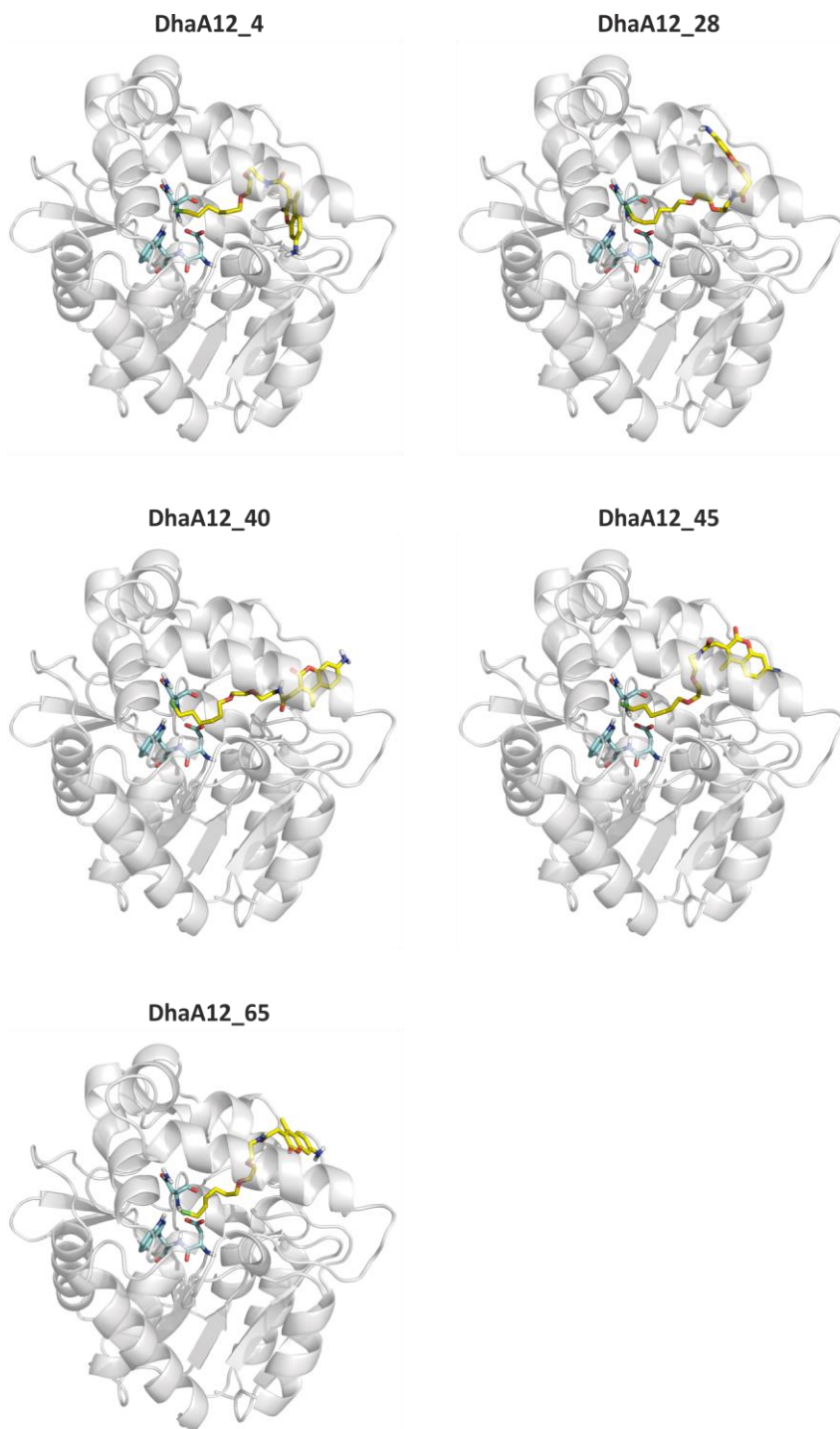
Supplementary Figure 8. Three lowest-energy conformations of the covalent linker. Linker is capped with ACE residue (atoms 59-64) covalently bound to the aspartic acid residue capped with NME (atoms numbered 47-52) and ACE (atoms 53-58) residues employed for the fragment parameterization. The atoms are numbered in concert with Supplementary Table 8.



Supplementary Figure 9. Five reactive binding modes of the probe bound in DbjA. Probe is visualized with yellow sticks and enzyme as grey cartoon. The catalytic nucleophile and the two halide-stabilizing residues are in cyan sticks.



Supplementary Figure 10. Three reactive binding modes of the probe bound in DhaA. Probe is visualized with yellow sticks and enzyme as grey cartoon. The catalytic nucleophile and the two halide-stabilizing residues are in cyan sticks.



Supplementary Figure 11. Five reactive binding modes of the probe bound in DhaA12. Probe is visualized with yellow sticks and enzyme as grey cartoon. The catalytic nucleophile and the two halide-stabilizing residues are in cyan sticks.

Supplementary Table 1. Characteristics of enzymes used in this study.

Enzyme	Mutations	Engineered region	T_m (°C) ^a	Reference
DhaA	None	None	50.5 ± 0.3	This study
DhaA +H272F	H272F	Catalytic base	NT ^b	¹⁹
DhaA07	ERB fragment + W141F + P153A	ERB fragment	unfolded	This study
DhaA08	ERB fragment + W141F + P153A + F155A	ERB fragment	35.0 ± 0.8	This study
DhaA09	ERB fragment + W141F + P153A + F155A + V256A	Main access tunnel	unfolded	This study
DhaA10	ERB fragment + W141F + P153A + F155A + V256A + A183V	Main access tunnel	40.5 ± 0.6	This study
DhaA11	ERB fragment + W141F + P153A + F155A + V256A + A183V + C187G	Main access tunnel	42.5 ± 0.8	This study
DhaA12	ERB fragment + W141F + P153A + F155A + V256A + A183V + C187G + G182R + K186G	Main access tunnel	44.6 ± 0.2	This study
DhaA12 +H283F	ERB fragment + W141F + P153A + F155A + V256A + A183V + C187G + G182R + K186G + H283F	Catalytic base	NT ^b	This study
DbjA	None	None	53.6 ± 0.6	^{20,21}
DbjA +H280F	H280F	Catalytic base	NT ^b	¹⁹

ERB fragment relates to the insertion of His-His-Thr-Glu-Val-Ala-Glu-Glu-Gln-Asp-His between the residues 141 and 142 of DhaA wild type. Cumulatively added mutations are in bold. The point mutation in the catalytic base (His272Phe, His283Phe and His280Phe) enables covalent binding of fluorescence probe required for time-dependent fluorescence experiments. ^a T_m – melting temperature; data represent mean values ± s.d. calculated from triplicate experiments ^bNT – not tested

Supplementary Table 2. Enantioselectivity of wild type and variants with β -bromoalkanes and α -bromoester.

Enzyme	<i>E</i> -value			
	2-Bromopentane	2-Bromohexane	2-Bromoheptane	Ethyl 2-bromopropionate
DhaA	8	4	2	72
DhaA08	5	4	2	163
DhaA10	9	11	2	> 200
DhaA11	8	12	2	> 200
DhaA12	7	11	10	> 200
DbjA^a	145	68	28	> 200

Data was fitted by nonlinear regression based on the simulation with the standard error of the fit between 5 and 25%. ^a data from²⁰.

Supplementary Table 3. Data collection and refinement statistics for the crystal structure of DhaA12.

DhaA12	
Data collection	
Space group	P2 ₁ 2 ₁ 2 ₁
Cell dimensions	
<i>a</i> , <i>b</i> , <i>c</i> (Å)	51.58, 68.69, 84.37
α , β , γ (°)	90.00, 90.00, 90.00
Resolution (Å)	31.39–1.78 (1.88–1.78) ^a
<i>R</i> _{merge}	8.4 (37)
<i>I</i> / σI	14.4 (4.2)
Completeness (%)	100.0 (99.9)
Redundancy	4.1 (4.1)
Refinement	
Resolution (Å)	1.78
No. reflections	34,658
<i>R</i> _{work} / <i>R</i> _{free}	0.176/0.207
No. atoms	
Protein	2,537
Chloride ion	1
Water	270
Non-H atoms	2,808
<i>B</i> -factors (Å ²)	
Protein	16.7
Ligand/ion	12.7
Water	24.5
R.m.s. deviations	
Bond lengths (Å)	0.007
Bond angles (°)	0.024

Parameters were obtained from a single crystal of DhaA12 protein.

^aThe highest-resolution shell is shown in parentheses.

Supplementary Table 4. Parameters characterizing the overall time-dependent fluorescence shift.

Enzyme	ν_0 (cm^{-1})	$\Delta\nu$ (cm^{-1})	τ_1 (ns) (A_1)	τ_2 (ns) (A_2)	τ_3 (ns) (A_3)	τ (ns)	% <i>obs.</i>
DhaA	23300±60	950±80	0.2 (310)	1.3 (340)	12.6 (200)	4.1±0.3	90±5
DhaA12	23300±70	1000±100	0.2 (400)	-	9.1 (400)	3.8±0.4	85±6
DbjA	23400±60	1300±140	< 0.1 (280)	1.4 (220)	11.0 (370)	2.8±0.3	62±9

ν_0 corresponds to the emission maximum of “time zero spectrum” which is a spectrum emitted from the completely non-relaxed Franck-Condon state and which was determined by the modified “time 0 estimation” as described previously¹⁹. The rest of the given parameters was obtained by the analysis of the time dependence of time resolved emission spectra (TRES): $\nu(\infty)$ stands for the emission maximum of the spectrum from fully relaxed state which was obtained by extrapolation of $\nu(t)$ to $t \rightarrow \infty$. $\Delta\nu$ represents the overall dynamic Stokes Shift derived as $\Delta\nu = \nu_0 - \nu(\infty)$. Multiexponential fitting of time evolution of the TRES peak maximum $\nu(t)$, and analysis of the autocorrelation curve $C(t)$: τ_i are the fitted relaxation times, A_i correspond to the amplitudes, τ is the integral relaxation time, and % *obs.* corresponds to the percentage of the solvent relaxation process captured with the given experimental time resolution of 30 ps. Four experiments were performed for DhaA and DbjA, and duplicate measurements were carried out in the case of DhaA12. Data represent mean values \pm s.d. τ_i and A_i parameters were gained by the non-linear least square fitting with 3-exponential function. Fitting procedure yielded standard deviation lower than 10% for all the parameters.

Supplementary Table 5. Parameters describing the dynamics and hydration of wild types and DhaA12 mutant.

Enzyme	Dynamics		Hydration	
	Integral relaxation time [ns] ^a	Integral B-factor of the tunnel mouth near dye [\AA^2] ^b	Dynamic Stokes shift [cm^{-1}] ^a	Average number of water molecules around dye ^b
DhaA	4.1± 0.3	132	950±80	6±2
DhaA12	3.8± 0.4	217	1000±100	6±2
DbjA	2.8± 0.3	315	1300±140	10±2

^a data from time-dependent fluorescence shift experiments; data represent mean values ± s.d. calculated from four experiments for DhaA and DbjA, and two measurements for DhaA12. ^b data from molecular dynamics simulations; data represent mean values ± s.d. calculated from 3,000 snapshots.

Supplementary Table 6. Variable residues in the second and the third shell of the active sites of DbjA and DhaA12.

Residues		Location
DbjA	DhaA12	
Phe66	Met69	Second shell
Gln102	His105	Second shell
Thr106	Ser109	Second shell
Met132	Ile135	Second shell
Ile185	Val188	Second shell
Val210	Leu213	Second shell
Leu230	Val235	Second shell
Val255	Ile258	Second shell
Ile44	Leu47	Third shell
Ala101	Ile104	Third shell
Ala109	Gly112	Third shell
Phe125	Cys128	Third shell
Ala233	Tyr236	Third shell
His234	Met237	Third shell
Ser256	Pro259	Third shell
Leu275	Ile278	Third shell

Supplementary Table 7. Atom types and charges for the fluorescent probe used in the simulations.

Atom number	Atom type	Charge
1	N2	-0.8691
2	H	0.3788
3	H	0.3788
4	CA	0.3555
5	CA	-0.2906
6	HA	0.1770
7	CA	-0.1881
8	HA	0.1741
9	CA	0.0162
10	CA	0.1939
11	CA	-0.2725
12	HA	0.1773
13	OA	-0.3635
14	CA	0.7418
15	O	-0.5652
16	CA	0.0595
17	CT	-0.1794
18	HC	0.0799
19	HC	0.0799
20	HC	0.0799
21	CA	-0.1896
22	CT	-0.0634
23	HC	0.0502
24	HC	0.0502
25	C	0.5745
26	O	-0.5863

Atom numbers are defined in Supplementary Fig. 7. Atom types accordingly to Cornell et al. force field⁶.

Supplementary Table 8. Atom types and charges for the covalent linker bound to the aspartic acid residue used in the simulations.

Atom number	Atom type	Charge
1	N	-0.4520
2	H	0.2592
3	CT	0.0703
4	H1	0.0632
5	H1	0.0632
6	CT	0.1685
7	H1	0.0333
8	H1	0.0333
9	OS	-0.4819
10	CT	0.1700
11	H1	0.0315
12	H1	0.0315
13	CT	0.1970
14	H1	0.0266
15	H1	0.0266
16	OS	-0.4681
17	CT	0.1421
18	H1	0.0196
19	H1	0.0196
20	CT	0.0397
21	HC	0.0104
22	HC	0.0104
23	CT	0.0190
24	HC	-0.0126
25	HC	-0.0126
26	CT	0.0131
27	HC	-0.0046
28	HC	-0.0046
29	CT	0.0142
30	HC	0.0252
31	HC	0.0252
32	CT	0.0353
33	H1	0.0768
34	H1	0.0768
35	OS	-0.3987
36	C	0.7481
37	O	-0.5573
38	CT	-0.2840
39	HC	0.0969
40	HC	0.0969
41	CT	0.1284
42	H1	0.0192
43	N	-0.4156
44	H	0.2718
45	C	0.5972
46	O	-0.5679

Atom numbers are defined in Supplementary Fig. 8. Atom types accordingly to Cornell et al. force field⁶.

Supplementary Table 9. Binding energies of individual binding modes of the fluorescent probe.

Enzyme	Binding mode				
	Enzyme-probe binding energy [kcal/mol]				
DbjA	DbjA_18	DbjA_21	DbjA_28	DbjA_30	DbjA_38
	-13±3	-11±2	-10±2	-19±2	-11±2
DhaA	DhaA_4	DhaA_10	DhaA_33	-	-
	-16±3	-21±2	-11±2		
DhaA12	DhaA12_4	DhaA12_28	DhaA12_40	DhaA12_45	DhaA12_65
	-23±3	-9±3	-9±3	-11±2	-8±1

Individual binding modes are depicted in Supplementary Fig. 9-11. Binding modes selected for further analysis are in bold. Data represent mean values ± s.d. calculated from 3,000 snapshots.

Supplementary references

1. Gordon, J. C. *et al. Nucleic Acids Res.* **33**, W368–371 (2005).
2. Dewar, M. J. S., Zoebisch, E. G., Healy, E. F. & Stewart, J. J. P. *J. Am. Chem. Soc.* **107**, 3902–3909 (1985).
3. Sanner, M. F. *J. Mol. Graph. Model.* **17**, 57–61 (1999).
4. Morris, G. M. *et al. J. Comput. Chem.* **19**, 1639–1662 (1998).
5. Solis, F. J. & Wets, R. J. B. *Math. Oper. Res.* **6**, 19–30 (1981).
6. Cornell, W. D. *et al. J. Am. Chem. Soc.* **117**, 5179–5197 (1995).
7. VanBeek, D. B., Zwier, M. C., Shorb, J. M. & Krueger, B. P. *Biophys. J.* **92**, 4168–4178 (2007).
8. Dupradeau, F.-Y. *et al. Phys. Chem. Chem. Phys.* **12**, 7821–7839 (2010).
9. Vanquelef, E. *et al. Nucleic Acids Res.* **39**, W511–517 (2011).
10. Hur, S., Kahn, K. & Bruice, T. C. *Proc. Natl. Acad. Sci. U. S. A.* **100**, 2215–2219 (2003).
11. Jorgensen, W. L., Chandrasekhar, J., Madura, J. D., Impey, R. W. & Klein, M. L. *J. Chem. Phys.* **79**, 926–935 (1983).
12. Hornak, V. *et al. Proteins* **65**, 712–25 (2006).
13. Darden, T., York, D. & Pedersen, L. *J. Chem. Phys.* **98**, 10089–10092 (1993).
14. Essmann, U. *et al. J. Chem. Phys.* **103**, 8577–8593 (1995).
15. Ryckaert, J.-P., Ciccotti, G. & Berendsen, H. J. C. *J. Comput. Phys.* **23**, 327–341 (1977).
16. Humphrey, W., Dalke, A. & Schulten, K. *J. Mol. Graph.* **14**, 33–8, 27–8 (1996).
17. Still, C., Tempczyk, A., Hawley, R. & Hendrickson, T. *J. Am. Chem. Soc.* **112**, 6127–6129 (1990).
18. Onufriev, A., Bashford, D. & Case, D. A. *Proteins* **55**, 383–394 (2004).
19. Jesenska, A. *et al. J. Am. Chem. Soc.* **131**, 494–501 (2009).
20. Prokop, Z. *et al. Angew. Chem. Int. Ed Engl.* **49**, 6111–6115 (2010).
21. Chaloupkova, R., Prokop, Z., Sato, Y., Nagata, Y. & Damborsky, J. *FEBS J.* **278**, 2728–2738 (2011).